

Field induced crossover of magnetic interaction and direct measurement of the magnetocaloric properties of $\text{La}_{0.4}\text{Pr}_{0.3}\text{Ca}_{0.1}\text{Sr}_{0.2}\text{MnO}_3$

Sagar Ghorai,¹ Ridha Skini,¹ Daniel Hedlund,¹
Petter Ström,² and Peter Svedlindh¹

¹Solid State Physics, Department of Materials Science and Engineering, Uppsala University, Box 534, 751 21 Uppsala, Sweden

²Applied Nuclear Physics, Department of Physics and Astronomy, Uppsala University, Box 516, SE-751 20 Uppsala, Sweden

Abstract:

$\text{La}_{0.4}\text{Pr}_{0.3}\text{Ca}_{0.1}\text{Sr}_{0.2}\text{MnO}_3$ has been investigated as a potential candidate for room temperature magnetic refrigeration. Results from X-ray powder diffraction reveal an orthorhombic structure with Pnma space group. The electronic and chemical properties have been confirmed by X-ray photoelectron spectroscopy and ion-beam analysis. A second-order paramagnetic to ferromagnetic transition was observed near room temperature (289 K). Owing to the formation of magnetic clusters at lower field a field induced crossover from long range to short range magnetic interaction was observed in the compound. A comparatively high value of the isothermal entropy change (3.08 J/kg-K at 2 T) is observed and the direct measurements of the adiabatic temperature change reveal a temperature change of 1.5 K for a magnetic field change of 1.9 T.

1. Introduction:

The need for reduced emission of greenhouse gases, emitted from conventional liquid gas refrigeration devices, has resulted in an increasing interest towards solid state refrigeration systems based on the magnetocaloric effect (MCE) [1]. Historically, in 1949, Giauque and MacDougall received the Nobel Prize for their achievement to reach a temperature below 1 K, using the magnetocaloric effect [2,3]. The next large breakthrough came in the end of the 90's, with the discovery of 'Giant' MCE and the development of a magnetic refrigerator using Gd as refrigerant by Ames laboratory and Astronautics Corporation of America, making the dream of a magnetic refrigerator possible [4].

Since then, several giant-magnetocaloric alloy-materials have been proposed as potential refrigerants for magnetic refrigeration [5–9]. Although these alloys show high adiabatic temperature changes (ΔT_{ad}) near room temperature, their corrosive properties and large thermal hysteresis limit their use in magnetic refrigeration. The perovskite manganites ($A_{1-x}B_xMnO_3$, where A is trivalent rare earth cation and B is divalent alkaline earth cation) are good candidates as magnetic refrigerants owing to their chemical stability, resistance to corrosion, negligible thermal hysteresis, large relative cooling power (RCP) and magnetic phase transitions near room temperature [10–13]. Substantial research work [14] has shown that the key factor for magnetic refrigeration is the adiabatic temperature change which is defined as [15],

$$\Delta T_{ad} = -\mu_0 \int_0^{H_{max}} \frac{T}{C_{p,H}} \left(\frac{\partial M}{\partial T} \right) dH, (1)$$

where μ_0 is free-space permeability, H_{max} is the final magnetic field, and $C_{p,H}$ is the heat capacity at constant pressure and field. Materials with higher magnetic moment and a Curie temperature (T_C) near room temperature are desirable for a room temperature magnetic refrigeration [16]. To satisfy these two requirements, in our previous work the non-magnetic La^{3+} ion was partially substituted with the magnetic Pr^{3+} ion in the $La_{0.7}Ca_{0.1}Sr_{0.2}MnO_3$ compound and an enhancement of total magnetic moment along with an enhanced isothermal entropy change and relative cooling power were observed in the compound $La_{0.5}Pr_{0.2}Ca_{0.1}Sr_{0.2}MnO_3$ [13]. As a consequence of the substitution, T_C also shifted from 343 K to 296 K [17,18].

It has been observed in studies using active magnetic regenerator (AMR) cycles, that a material with a large isothermal entropy change in a narrow temperature span demonstrates significantly lower cooling power than a material with a moderate isothermal entropy change in a wide temperature span [14,16]. Hence, research should focus on finding materials with a high ΔT_{ad} in a broad temperature span to enhance the cooling power in real applications. This is the advantage of oxide materials, their broad second order magnetic phase transition results in a broad temperature span in which the magnetic cooling is effective. Although to trade-off with the high value of heat capacity,

a sufficiently large magnetic field is required to run the AMR cycle. In recent years there is a huge progress in magnetocaloric research using pulsed magnetic field as high as 60 T [19–23]. So, there is a huge possibility to use the oxides in AMR or similar refrigeration cycle in future with a high magnetic field.

In this work, we have investigated the structural, electronic, magnetic, magnetocaloric and universal scaling properties of the $\text{La}_{0.4}\text{Pr}_{0.3}\text{Ca}_{0.1}\text{Sr}_{0.2}\text{MnO}_3$ (**LP3**) compound. Along with isothermal entropy change, the adiabatic temperature change was also measured in the **LP3** compound and an estimation of required magnetic field was made for the application of the material in a real AMR cycle. The observed value of adiabatic temperature change is relatively high compared to most of the oxides reported so-far except $\text{La}_{0.67}\text{Ca}_{0.33}\text{MnO}_3$ which shows a first order magnetic transition near 268 K [24]. Thus, **LP3** has the advantage of having the magnetic phase transition near room temperature. A field induced change of magnetic interaction was also observed in this compound. Using a quantitative method derived from magnetocaloric exponent (n), this change of magnetic interaction-range was demonstrated in this work.

2. Experimental details:

The **LP3** compound was prepared by solid-state reaction as described in our previous work [13]. The structural properties of the sample were characterized by X-ray powder diffraction (**XRPD**) at room temperature using $\text{Cu-K}\alpha$ radiation (Bruker D8-advance diffractometer) by steps of 0.012° with a delay time of 10 seconds per step. The elemental analysis of the **LP3** sample was performed by Rutherford backscattering spectrometry (RBS) with 2 MeV $^4\text{He}^+$ and 10 MeV $^{12}\text{C}^{3+}$ beams, as well as time-of-flight elastic recoil detection analysis (ToF-ERDA) [25] with 36 MeV $^{127}\text{I}^{8+}$. The beam was hitting the sample at 5° incidence angle with respect to the surface normal for both RBS measurements, and the energy detector was placed at a backscattering angle of 170° . The sample was wiggled within a 2° interval to average out possible channelling effects in grains. For ToF-ERDA the incidence angle was $23^\circ \pm 1^\circ$ with respect to the sample surface, and recoils were detected at 45° . X-ray photoelectron spectroscopy (**XPS**) was used to analyze the oxidation state of the sample. A “PHI Quantera II” system with an $\text{Al-K}\alpha$ X-ray source and a hemispherical electron energy analyzer with a pass energy of 26.00eV was used to record the XPS spectra. Pre-sputtering with Ar-ion of 200 eV for 12 seconds was done on the sample before collecting the XPS spectra in order to remove surface impurities without affecting the sample’s properties. The magnetic measurements were performed in a Quantum Design MPMS XL in the temperature range from 390 K to 5 K with a maximum field of 5 T. The adiabatic temperature change (ΔT_{ad}) were measured in steps of 0.1 T up to 1.90 T in a home-built device at Technical University of Darmstadt Functional Materials [26].

3. Results and discussion:

3.1. Crystal structure:

The XRPD pattern of the **LP3** sample is shown in **Figure 1(a)**. The Rietveld refinement (using the Fullprof program [27]) of the XRPD pattern confirms orthorhombic structure with Pnma space group for the sample, similar as previously reported for $\text{La}_{0.5}\text{Pr}_{0.2}\text{Ca}_{0.1}\text{Sr}_{0.2}\text{MnO}_3$ [13]. No other significant phases have been observed from the XRPD pattern. Details of the lattice parameters are listed in **Table 1**. For a typical rhombohedral structure, the value of the Goldschmidt tolerance factor ($t_G = \frac{r_A + r_O}{\sqrt{2}(r_B + r_O)}$, where r_A , r_B and r_O are the ionic radii of A, B site and oxygen ions, respectively) is $0.96 < t_G < 1$, while for an orthorhombic structure, the value of t_G is < 0.96 [28]. For the **LP3** compound the calculated value of t_G is 0.92, which resembles the observed orthorhombic structure of the compound.

Table 1 Lattice parameters and bond information from XRPD pattern	
Compound	$\text{La}_{0.4}\text{Pr}_{0.3}\text{Ca}_{0.1}\text{Sr}_{0.2}\text{MnO}_3$
Phase	Orthorhombic (Pnma)
Lattice parameters (Å)	$a = 5.46124(6)$ $b = 7.71813(8)$ $c = 5.49213(6)$
Bond lengths (Å)	Mn-O1: 1.9598(13) Mn-O2: 1.952(4)
Bond angles (°)	Mn-O1-Mn: 159.9(5) Mn-O2-Mn: 165.4(4)
Rietveld Refinement Parameters [29]	$R_p = 5.56$, $R_{WP} = 7.64$, $R_B = 6.19$

3.2. Electronic Structure:

In manganites, with different valence states of Mn, different exchange interactions exist; Mn^{3+} - O^{2-} - Mn^{4+} gives rise to ferromagnetic (**FM**) double-exchange interaction and Mn^{3+} - O^{2-} - Mn^{3+} (or Mn^{4+} - O^{2-} - Mn^{4+}) gives rise to antiferromagnetic (**AFM**) super-exchange interaction [30]. Thus, the average Mn-oxidation state plays a crucial role in determining the influence of FM and AFM interactions. XPS has been used to determine the oxidation state of the **LP3** compound and the results are shown in **Figure 1(b)**. The observed $\text{Mn}^{3+}/\text{Mn}^{4+}$ ratio was 2.3(7), which is comparable to the expected value 2.33. The

lack of satellite peaks confirms the absence of any Mn^{2+} state [31]. The observed spin-orbit splitting between $\text{Mn-}2p_{1/2}$ and $\text{Mn-}2p_{3/2}$ was 11.62 eV which indicates a decrease of the spin-orbit splitting with increasing La^{3+} substitution compared to the result for our previously reported compound $\text{La}_{0.5}\text{Pr}_{0.2}\text{Ca}_{0.1}\text{Sr}_{0.2}\text{MnO}_3$ [13].

The Mn-3s spectra is shown in **Figure 1(b)**. The parallel and anti-parallel coupling of the spins of 3s-core holes and 3d electrons give rise to two distinct peaks (high spin and low spin state at lower and higher binding energy, respectively) in the Mn-3s spectrum [32,33]. Beyreuther *et. al.* [34] derived a linear relationship between the Mn-valence state (v_{Mn}) and the exchange splitting (ΔE_{3s}) of the two Mn-3s peaks,

$$v_{\text{Mn}} = 9.67 - 1.27\Delta E_{3s} / \text{eV}. \quad (2)$$

The observed energy splitting ($\Delta E_{3s} = 5.1(5)$ eV), gives $v_{\text{Mn}} = 3.2(5)$, which is comparable with the expected $v_{\text{Mn}} = 3.33$ for the **LP3** compound.

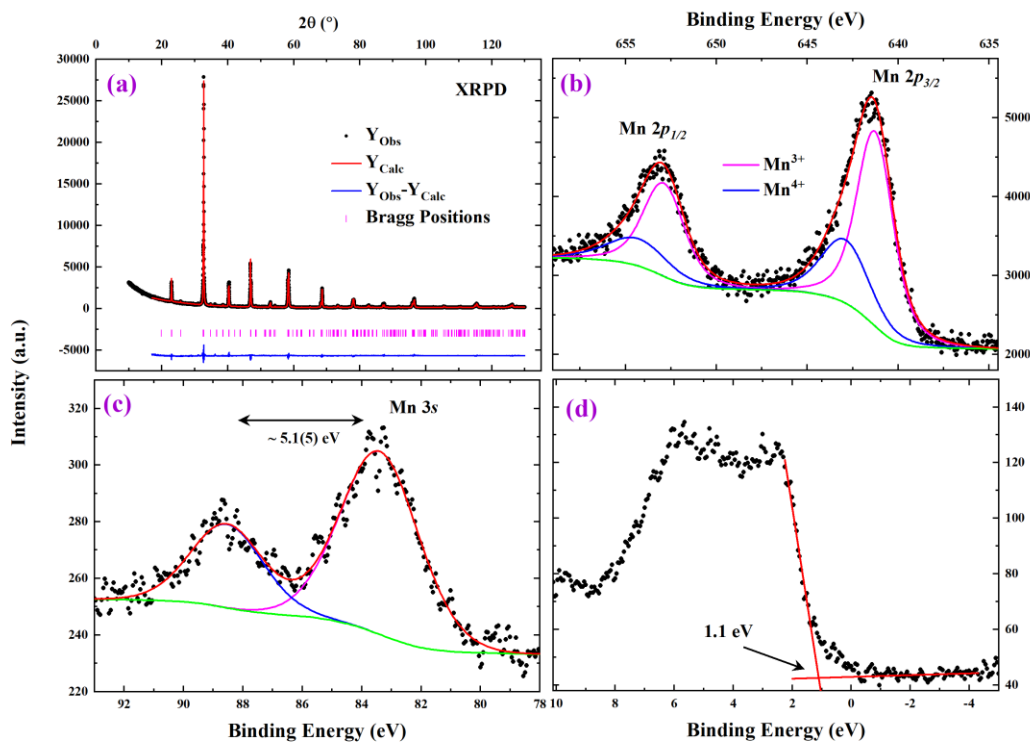


Figure 1(a) Rietveld refined XRPD pattern and XPS spectra of **(b)** Mn-2p, **(c)** Mn-3s and **(d)** valence band of the **LP3** compound.

The valence band (VB) spectrum of the **LP3** compound was recorded in its paramagnetic state (~ 295 K) and is shown in **Figure 1(d)**. The primary contributions of $\text{O}2p$, $\text{Mn}3d$ and $\text{Pr}4f$ orbitals are present in the VB spectrum. The observed valence band offset is ~ 1.1 eV calculated from the linear regression

fit along the leading edge of the valence band spectra [35,36]. Due to the crystal field effect a distinct feature of the $Mn3d(e_g)$ orbital is expected [33,37,38] near $\sim 0.5\text{eV}$ in the ferromagnetic region. However, as this VB spectrum was recorded at room temperature (paramagnetic state) the $Mn3d(e_g)$ state is less pronounced. Thus, a low temperature XPS along with theoretical calculations is required to make clear identification of the valence band states.

3.2. Ion Beam Analysis (IBA):

Raw ToF-ERDA data is shown in **Figure 2(a)**. In addition to the expected sample constituents, C, Si and H are detected. The signal labelled “Si” may include counts attributable to Al, but is processed as Si below.

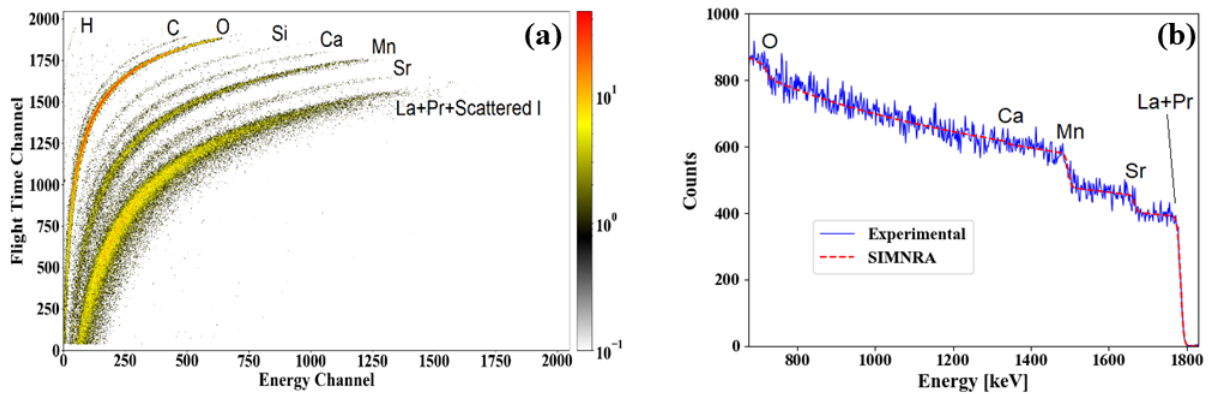


Figure 2(a) Raw ToF-ERDA data from sample LP3. **(b)** ^4He RBS data with overlaid SIMNRA calculated spectrum for sample LP3.

Depth profiling of the ToF-ERDA data with Potku [39] and integration from depth 1.5×10^{17} at/cm² to 3×10^{18} at/cm² yielded a first estimation of the sample composition while ignoring La and Pr, whose signals are obscured by primary ions scattering into the detector. The $^4\text{He}^+$ RBS data was treated with SIMNRA [40]. **Figure 2(b)** shows the experimental data and a calculated spectrum based on a fit of the fractions of Mn, Sr, La and Pr which improves the quality of the information about the relative amounts of these elements. La and Pr were not separable with $^4\text{He}^+$ backscattering, so the La/Pr-ratio was fixed to the expected value for the fitting. The full composition of the sample was calculated from the ^4He -RBS and ToF-ERDA results by taking the ratios of La, Pr and Sr to Mn from RBS and those of H, C, O, Si and Ca to Mn from ToF-ERDA. The resulting atomic concentrations are given in **Table 2**. The number of counts for which the H, C, O, Si, Ca and Mn fractions were calculated from the ToF-ERDA data are approximately 40 (H), 300 (C), 18000 (O), 400 (Si), 1000 (Ca) and 8000 (Mn). This gives rise to statistical uncertainties, which are treated further below. For H, the main error comes from ion-induced gas release during the measurement as well as an uncertainty in the detection efficiency. A

check for ion-induced release of O was performed by dividing the measurement into chronological slices and tracking the time-evolution of the O-signal. No decrease with time was observed, and as such the measurement did not suffer from any noticeable ion-induced release of O. The error here comes rather from the statistical uncertainty in the Mn-signal, which is around 1% and an uncertainty of approximately 5% in the relative detection efficiency. In addition to these error sources, the C, Si and Ca signals include a non-negligible number of background counts. A region of similar size as that giving rise to the Ca signal, but selected between the Ca and Mn regions contains approximately 20-30 counts, i.e. around 5-10% of the C and Si signals and 2-3% of the Ca signal. Combining these error sources yields the error margins in **Table 2**. For Mn, Sr and La+Pr the relative statistical uncertainties in the number of counts from RBS are 3%, 5% and 1%, respectively. The ratio (La+Pr)/(Sr+Ca) is measured as 2.14 ± 0.21 . The error in the fraction of Mn, which is used as a normalization element to combine the RBS and ERDA data, is included here in addition to the explicit errors in the individual elemental concentrations.

Table 2 Atomic percentages of the **LP3** sample as measured by ToF-ERDA (H, C, O, Si, Ca) and RBS (Mn, Sr, La, Pr). * The error in the total amount of La+Pr is ± 0.4 at. % ($\pm 3\%$ relative) due to the statistical uncertainty in the number of counts attributed to Mn, while the individual fractions of La and Pr are approximate (see Fig. 3).

Element	Expected Atomic %	Observed Atomic %
La	8	8.2*
Pr	6	6.1*
Ca	2	2.4(2)
Sr	4	4.3(2)
Mn	20	19.1(6)
O	60	57(3)
H	0	0.7(4)
C	0	1.0(1)
Si	0	1.2(1)

In order to verify that the La/Pr ratio is close to the expected value, the RBS data obtained with $^{12}\text{C}^{3+}$ was compared to SIMNRA calculations where either only La, only Pr or both La and Pr with the expected ratio were considered for the La+Pr signal. In all three cases, the entire spectrum can be well

reproduced, except for the La+Pr signal edge around 7.1 keV, which is reproduced by a La/Pr ratio of 4/3 as shown in **Figure 3**.

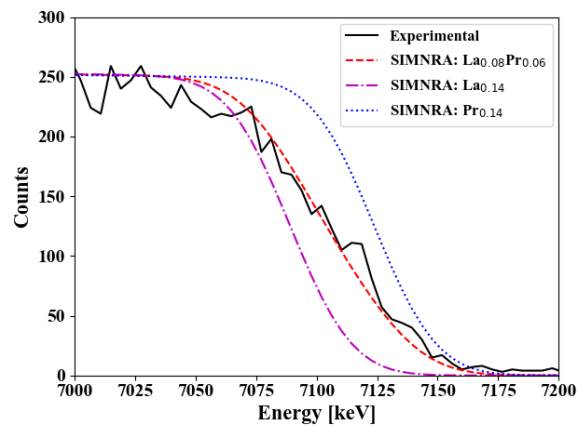


Figure 3 $^{12}\text{C}^{3+}$ RBS data for the La+Pr signal edge, verifying that the expected ratio reproduces the measured data while calculations using only La or Pr do not.

3.3. Magnetic properties:

The temperature dependence of the field cooled magnetization ($M(T)$) using an applied magnetic field of 0.01 T is presented in **Figure 4(a)**. The $M(T)$ curve reveals that the sample exhibits a paramagnetic-ferromagnetic transition at a temperature (T_C) close to room temperature. The value of T_C determined from the $\partial M/\partial T$ versus T curve (not shown here) was found to be 289 K, which presents a main factor in room temperature cooling technology [41,42]. A linear temperature dependence of the inverse susceptibility was observed in the paramagnetic region of the **LP3** compound. From the Curie-Weiss fit the extracted Weiss temperature is 291K, which is close to the value T_C - Moreover, no Griffiths phase like singularity was observed in **LP3** compound unlike for our previously reported $\text{La}_{0.5}\text{Pr}_{0.2}\text{Ca}_{0.1}\text{Sr}_{0.2}\text{MnO}_3$ compound [13].

We have studied the magnetic hysteresis by varying the applied magnetic field from -2 to 2 T at 100 K (in ferromagnetic region) and 285 K (near T_C) (**Figure 4 (c)**); no hysteresis was detected indicating negligible energy loss during the magnetization-demagnetization process. This result represents an advantage as well a reason for the choice of oxide materials as refrigerant materials in MCE based cooling systems compared to giant magnetocaloric materials with a first order magnetic transition (**FOMT**) which usually show undesirable magnetic and thermal hysteresis making them unsuitable for magnetic refrigeration [43-45].

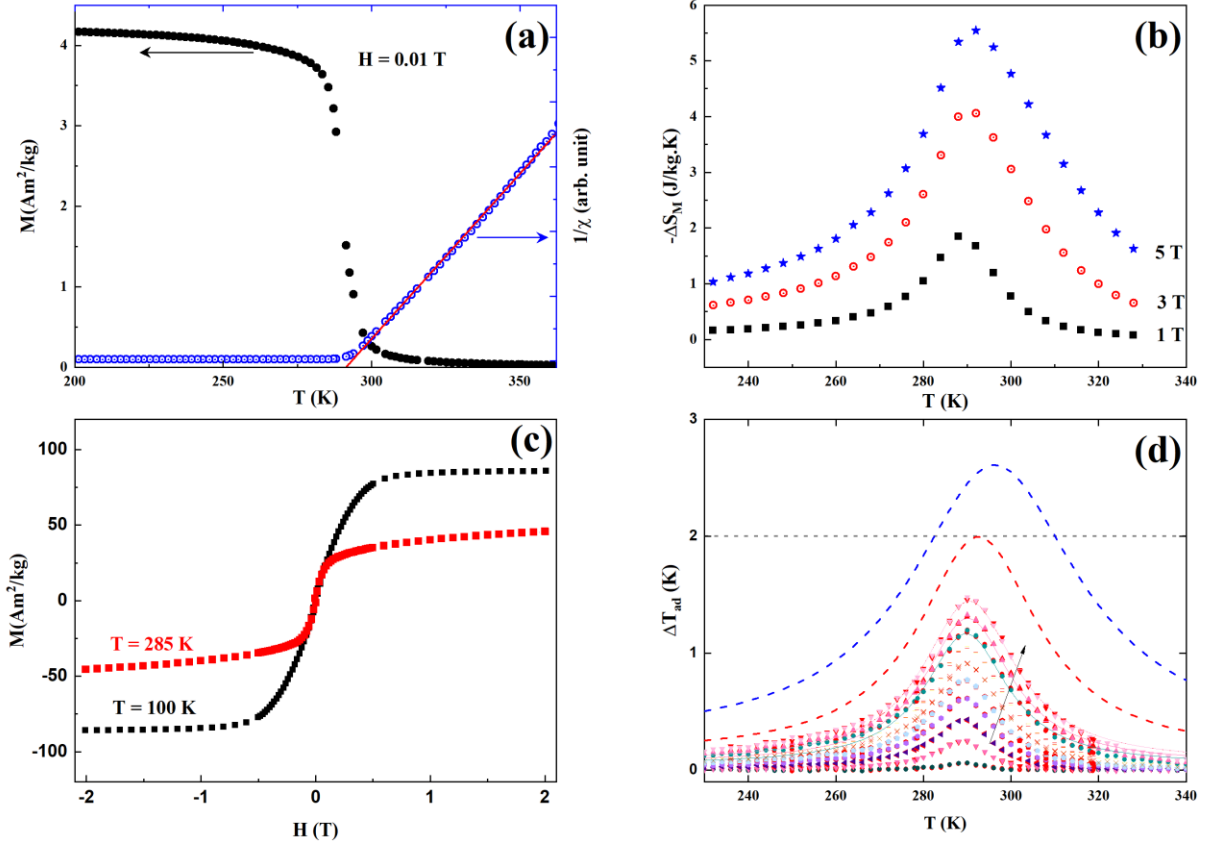


Figure 4: (a) Magnetization and inverse susceptibility as a function of temperature. (b) Isothermal entropy change as a function of temperature for different $\mu_0 H_f$ values. (c) The magnetization versus magnetic field in the ferromagnetic region. (d) ΔT_{ad} versus temperature for different $\mu_0 H_f$ values between 0.1 and 1.9 T in steps of 0.2 T. The dashed (--) upper curves corresponds to extrapolated values for $\mu_0 H_f = 3$ T (red) and 5 T (blue).

3.4. Magnetocaloric properties:

We have calculated the magnetic entropy change from magnetization isotherms using Maxwell's relationship defined as [16],

$$\Delta S_M = \mu_0 \int_0^{H_f} \left(\frac{\partial M}{\partial T} \right)_H dH. \quad (3)$$

The magnetic entropy change as a function of temperature for different $\mu_0 H_f$ values can be seen in **Figure 4 (b)**. The value of the isothermal entropy-change increases with increasing magnetic field and achieves its highest value near T_C . The maximum $-\Delta S_M$ value was found to be 3.08 J /kg-K under an applied magnetic field of 2 T. This value is large compared to that obtained for some other manganite materials [42,46,47]. It is important to realise the temperature span in which the cooling process will be effective. For this purpose, the RCP is introduced as,

$$RCP = -\Delta S_M^{max} \times \Delta T_{FWHM}, \quad (4)$$

where $-\Delta S_M^{max}$ is the maximum value of isothermal entropy change and ΔT_{FWHM} is the full width at half maximum of the isothermal entropy change curve with respect to temperature. The **LP3** compound shows a high value of RCP, 83.3 J/kg at $\mu_0 H_f = 2T$.

Figure 4(d) shows the temperature dependence of ΔT_{ad} measured for different $\mu_0 H_f$ values. The maximum of ΔT_{ad} is 1.5 K for a magnetic field change of $\mu_0 H_f = 1.9$ T. Also, in the figure we have put the condition $\Delta T_{ad} = 2$ K as a dotted line as Engelbrecht and Bahl [14] have shown that cooling will cease if ΔT_{ad} drops below 2 K. We have also fitted the ΔT_{ad} versus temperatures curves using a Lorentzian profile to simulate the response of the material for higher $\mu_0 H_f$ values,

$$\Delta T_{ad}(\mu_0 H_f) = T_0 + \frac{2Aw}{\pi(4(T-T_c)^2 + w^2)}, \quad (5)$$

where T_0 is a temperature offset, A is related to the area under the curve and w is the FWHM. Fitting **Equation (5)** to different $\mu_0 H_f$ reveal that all parameters (T_0 , A , w , T_c) are linearly dependent to $\mu_0 H_f$, and for the simulated data of $\mu_0 H_f = 3$ T and $\mu_0 H_f = 5$ T we thus used parameters from these fits.

Generally, ΔT_{ad} found in oxide materials is relatively low compared to that of metallic and intermetallic magnetocaloric materials due to its comparably high specific heat. Near T_c , ΔT_{ad} and ΔS_M are related by a simple relation [48],

$$\Delta T_{ad} = -\frac{T_c}{C_H(T_c)} \Delta S_M, \quad (6)$$

where $C_H(T_c)$ is the heat capacity at constant magnetic field. Using this relation for the **LP3** compound the estimated heat capacity near T_c is around 574 J/kg-K at 1.9T field. As a comparison with Gd, the value of $C_H(T_c)$, is ~320 J/kg-K at 1.5 T field [49].

Considering the requirement $\Delta T_{ad} > 2$ K, RCP should only be considered between 282 and 310 K, giving $RCP_{\Delta T_{ad} > 2K} = 195.8$ J/kg for $\mu_0 H_f = 5$ T. This is one obvious reason that one should calculate RCP using the effective temperature span from adiabatic temperature change in order to avoid overestimation of RCP. In **Table 3**, the values of $-\Delta S_M^{max}$ and ΔT_{ad} are compared for some of the manganite-oxides having T_c near room temperature as a comparison with **LP3** compound.

Table 3: MCE values of magnanite-oxides with T_C near room temperature					
Compound	T_C (K)	$\mu_0 H_f$ (T)	$-\Delta S_M^{max}$ (J/kg-K)	ΔT_{ad} (K)	Reference
$\text{La}_{0.4}\text{Pr}_{0.3}\text{Ca}_{0.1}\text{Sr}_{0.2}\text{MnO}_3$	289	1.9	2.98	1.5	This work
$\text{La}_{0.5}\text{Pr}_{0.2}\text{Ca}_{0.1}\text{Sr}_{0.2}\text{MnO}_3$	296	2	1.82	-	[13]
$\text{La}_{0.2}\text{Pr}_{0.5}\text{Sr}_{0.3}\text{MnO}_3$	299	1.8	1.95	1.2	[50]
$\text{La}_{0.4}\text{Pr}_{0.3}\text{Sr}_{0.3}\text{MnO}_3$	337	1.8	1.91	1.33	[50]
Gd	294	2	~ 5	~ 5.8	[8]
$\text{La}_{0.6}\text{Ca}_{0.4}\text{MnO}_3$	~268	0.7	1.8	0.54	[15]
$\text{La}_{0.67}\text{Ca}_{0.33}\text{MnO}_3$	268	2.02	~6.5	2.4	[24]
$\text{La}_{0.7}\text{Ca}_{0.15}\text{Sr}_{0.15}\text{MnO}_3$	338	2	0.925	~1.26	[51]

3.5. Scaling analysis:

The study of critical behaviour provides crucial information of spin interactions in the material. The order of the magnetic transition is verified using the Banerjee criterion, which is based on the Arrott plots (M^2 versus H/M) [46,47,52]. As shown in **Figure 5 (a)**, the positive slopes of the M^2 versus H/M curves indicate a second-order phase transition. For a typical second-order phase transition, the critical behaviour of the material is decided by the dimensionality, range of interactions and symmetry of the order parameter [53]. Several universality classes are defined on the basis of the critical exponents δ , β and γ , which related to the magnetization isotherm at T_C , spontaneous magnetization (M_{sp}) and initial susceptibility (χ) by the following relations [53,54],

$$M(H, T) \propto H^{1/\delta}; T = T_C, \quad (7)$$

$$M_{sp}(0, T) \propto (-\varepsilon)^\beta; T < T_C, \quad (8)$$

$$\frac{1}{\chi}(0, T) \propto \varepsilon^\gamma; T > T_C, \quad (9)$$

where $\varepsilon = \frac{T-T_C}{T_C}$. Based on the Arrott-Noakes equation of state, a power law can be derived for the field dependence of $-\Delta S_M^{max}$ [53,55,56],

$$-\Delta S_M^{max} \propto H_f^n, \quad (10)$$

where n depends on the critical exponents as,

$$n = 1 + \{(\beta - 1)/(\beta + \gamma)\}. \quad (11)$$

In **Table 4**, the different universal classes are defined on the basis of the critical exponents described above.

Universal class	δ	β	γ	n	Reference
Mean-Field (MF)	3.0	0.5	1	0.667	[57]
3D-Heisenberg	4.8	0.365	1.336	0.627	[57]
3D-Ising	4.82	0.325	1.24	0.569	[57]
Tricritical MF	5.0	0.25	1.0	0.4	[57]
LP3 (low field)	3.19(2)	-	-	0.687(7)	This work
LP3 (high field)	5.35(2)	-	-	0.583(2)	This work

The magnetization isotherm recorded at T_C and $-\Delta S_M^{max}$ were fitted to the **Equations (7) and (10)**, respectively (shown in **Figure 5 (b) and (c)**). From the fitting it is clear that the power law equations are not able to account for the full magnetic field range although the intrinsic field is considered in order to avoid the demagnetization field effect at lower fields [58]. The fit at lower magnetic fields (intrinsic field range 0.4×10^5 A/m to 10×10^5 A/m) resembles the behaviour expected for long-range mean-field like interactions, while at higher magnetic fields (intrinsic field range 25×10^5 A/m to 39×10^5 A/m) it seems like short-range 3D-Ising/Heisenberg interactions best describes the experimental results. This type of field induced crossover has previously been observed in the $\text{La}_{0.7}\text{Pb}_{0.3}\text{MnO}_3$ [59]. The long-range interaction at lower fields is the result of cluster formation of the atomic spins due to magnetic disorder with respect to the exchange interactions. This cluster effect breaks down at higher fields and the atomic spins couples individually to the magnetic field.

There could be another possibility of having this power law violation. If the magnetic transition is not a pure second-order phase transition then the power law equations described above are not valid. The Banerjee criterion is based on the mean field approximation, thus not applicable for all 3D-systems [60]. To avoid confusion relating to the magnetic phase transition, a quantitative criterion of the exponent n was calculated following Jia Yan Law *et al.* [60], where n (using **Equation (10)**) is expressed as,

$$n(T, \mu_0 H_f) = \frac{d \ln(|\Delta S_M^{max}(T, \mu_0 H_f)|)}{d \ln(H_f)}. \quad (12)$$

According to this criterion, for a first-order magnetic transition a value $n > 2$ should be observed near T_C [60] and for a second-order transition the n value tends to 1 at $T \ll T_C$ and it approaches 2 at $T \gg T_C$ [61]. From **Figure 5 (d)**, using the quantitative criterion for n , it is evident that **LP3** compound shows a second-order phase transition. Also, near T_C , the field induced change of the value of n confirms the previous assumption of the transition from long-range to short-range magnetic interactions owing to the break-down of magnetic cluster with increasing field.

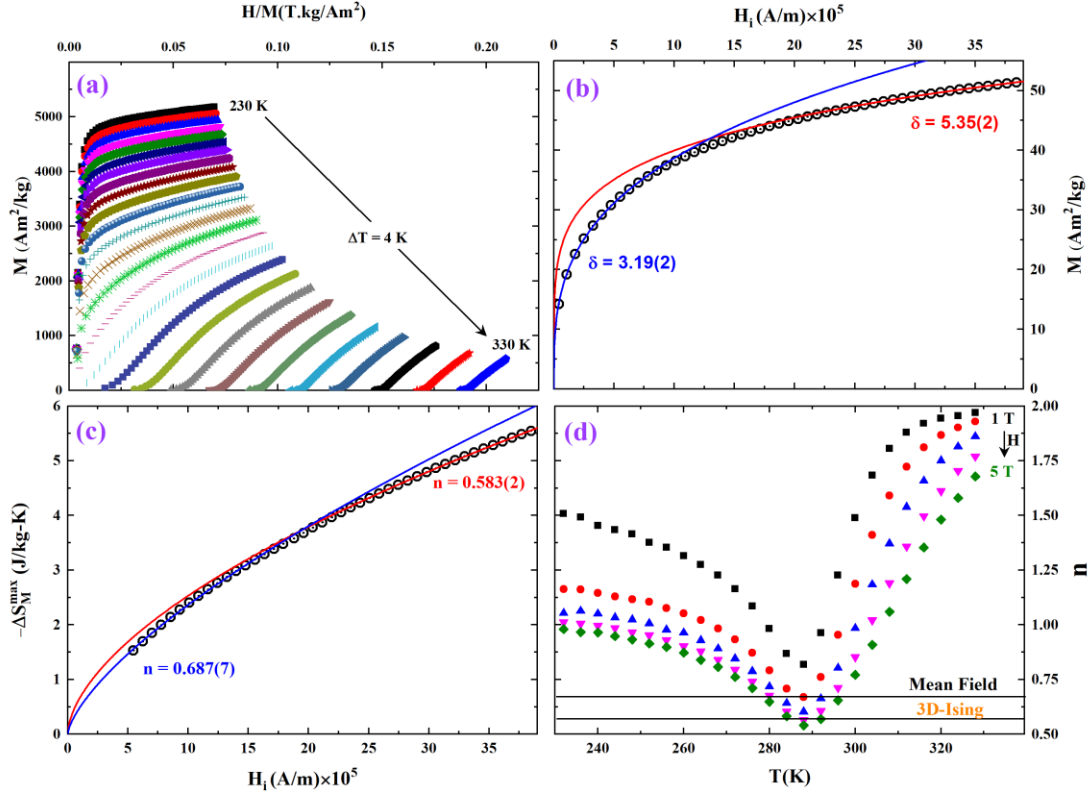


Figure 5 (a) Arrott plots at different temperatures. (b) Magnetization isotherm and (c) $-\Delta S_M^{max}$ versus intrinsic field at T_C . The red (blue) curve indicates a data fit assuming a 3D-Ising (mean-field) mode.. (d) variation of critical exponent n with magnetic field and temperature.

4. Conclusions:

A detailed analysis of the crystal structure, chemical composition, oxidation state, magnetic and magnetocaloric (direct and indirect) properties of the **LP3** compound has been reported here. An orthorhombic structure was observed from X-ray powder diffraction patterns, while the chemical stoichiometry and oxidation states were confirmed by the IBA and XPS techniques. A second-order magnetic phase transition was confirmed using the Banerjee criterion and the quantitative criterion based on the exponent n . The magnetization isotherm recorded at T_C and the field dependence of $-\Delta S_M^{max}$ did not follow the power law equations suggested for a second-order phase transition. This violation can be related to the field induced transition from long-range to short-range magnetic interactions governed by the formation of spin-clusters at lower magnetic fields.

A transition temperature near room temperature and the high value of isothermal entropy change and adiabatic temperature change over a wide temperature span (~ 40 K), makes **LP3** a potential candidate for magnetic refrigeration near room temperature. However, for a material to be useful as a magnetocaloric material near room temperature ΔT_{ad} needs to be larger than 2 K [14], otherwise cooling might cease. In the **LP3** compound, the magnetic field needs to be about 3 T for $\Delta T_{ad} = 2$ K.

However, the useful temperature span of the material in a field of 5 T is quite large and estimated to be between 282 K and 310 K.

Acknowledgement:

The Swedish Foundation for Strategic Research (SSF, contract EM-16-0039) supporting research on materials for energy applications is gratefully acknowledged. Infrastructural grants by VR-RFI (#2017-00646_9) and SSF (contract RIF14-0053) supporting accelerator operation are gratefully acknowledged. The authors are thankful to Vitalii Shtender for recording the XRPD data as well as to Konstantin Skokov for assistance in measuring the adiabatic temperature change.

References:

- [1] V.K. Pecharsky, K.A. Gschneidner, Giant Magnetic Effect in $\text{Gd}_5(\text{Si}_2\text{Ge}_2)$, *Phys. Rev. Lett.* 78 (1997) 4494–4497. <https://doi.org/10.1103/PhysRevLett.78.4494>.
- [2] W.F. Giaque, D.P. MacDougall, Attainment of temperatures below 1° absolute by demagnetization of $\text{Gd}_2(\text{SO}_4)_3 \cdot 8\text{H}_2\text{O}$ [12], *Phys. Rev.* 43 (1933) 768. <https://doi.org/10.1103/PhysRev.43.768>.
- [3] J.C.H. M. Balli, C. Mahmed, O. Sari, F. Rahali, Engineering Of The Magnetic Cooling Systems: A Promising Research Axis For Environment And Energy Saving, *World Eng. Conv.* (2011) hal-01185990. <https://hal.archives-ouvertes.fr/hal-01185990> (accessed March 30, 2020).
- [4] C. Zimm, A. Jastrab, A. Sternberg, V. Pecharsky, K. Gschneidner, M. Osborne, I. Anderson, Description and Performance of a Near-Room Temperature Magnetic Refrigerator, in: *Adv. Cryog. Eng.*, Springer US, 1998: pp. 1759–1766. https://doi.org/10.1007/978-1-4757-9047-4_222.
- [5] A. Yan, K.-H. Müller, L. Schultz, O. Gutfleisch, Magnetic entropy change in melt-spun MnFePGe (invited), *J. Appl. Phys.* 99 (2006) 08K903. <https://doi.org/10.1063/1.2162807>.
- [6] V.K. Pecharsky, A.P. Holm, K.A. Gschneidner, R. Rink, Massive Magnetic-Field-Induced Structural Transformation in Gd_5Ge_4 and the Nature of the Giant Magnetocaloric Effect, *Phys. Rev. Lett.* 91 (2003) 197204. <https://doi.org/10.1103/PhysRevLett.91.197204>.
- [7] A. Fujita, S. Fujieda, Y. Hasegawa, K. Fukamichi, Itinerant-electron metamagnetic transition and large magnetocaloric effects in $\text{La}(\text{Fe}_x\text{Si}_{1-x})_{13}$ compounds and their hydrides, *Phys. Rev. B.* 67 (2003) 104416. <https://doi.org/10.1103/PhysRevB.67.104416>.
- [8] V.K. Pecharsky, K.A. Gschneidner, Jr., Giant Magnetocaloric Effect in $\text{Gd}_5\text{Si}_2\text{Ge}_2$, *Phys. Rev. Lett.* 78 (1997) 4494–4497. <https://doi.org/10.1103/PhysRevLett.78.4494>.
- [9] K.H.J. Buschow, F.R. De Boer, O. Tegus, E. Bru, Transition-metal-based magnetic refrigerants for room-temperature applications, *Nature.* 415 (2002) 150–152. www.nature.com

- (accessed April 6, 2020).
- [10] R. Szymczak, R. Kolano, A. Kolano-Burian, V.P. Dyakonov, H. Szymczak, Giant Magnetocaloric Effect in Manganites, *Acta Phys. Pol. A.* 117 (2010) 203–206. <https://doi.org/10.12693/APhysPolA.117.203>.
- [11] P. Sande, L.E. Hueso, D.R. Miguéns, J. Rivas, F. Rivadulla, M.A. López-Quintela, Large magnetocaloric effect in manganites with charge order, *Appl. Phys. Lett.* 79 (2001) 2040–2042. <https://doi.org/10.1063/1.1403317>.
- [12] M.-H. Phan, S.-C. Yu, N.H. Hur, Y.-H. Jeong, Large magnetocaloric effect in a $\text{La}_{0.7}\text{Ca}_{0.3}\text{MnO}_3$ single crystal, *J. Appl. Phys.* 96 (2004) 1154–1158. <https://doi.org/10.1063/1.1762710>.
- [13] R. Skini, S. Ghorai, P. Ström, S. Ivanov, D. Primetzhofer, P. Svedlindh, Large room temperature relative cooling power in $\text{La}_{0.5}\text{Pr}_{0.2}\text{Ca}_{0.1}\text{Sr}_{0.2}\text{MnO}_3$, *J. Alloys Compd.* 827 (2020) 154292. <https://doi.org/10.1016/j.jallcom.2020.154292>.
- [14] K. Engelbrecht, C.R.H. Bahl, Evaluating the effect of magnetocaloric properties on magnetic refrigeration performance, *J. Appl. Phys.* 108 (2010) 123918. <https://doi.org/10.1063/1.3525647>.
- [15] A.R. Dinesen, S. Linderoth, S. Mørup, Direct and indirect measurement of the magnetocaloric effect in a $\text{La}_{0.6}\text{Ca}_{0.4}\text{MnO}_3$ ceramic perovskite, *J. Magn. Magn. Mater.* 253 (2002) 28–34. [https://doi.org/10.1016/S0304-8853\(01\)00941-6](https://doi.org/10.1016/S0304-8853(01)00941-6).
- [16] J. Lyubina, Magnetocaloric materials for energy efficient cooling, *J. Phys. D. Appl. Phys.* 50 (2017) 053002. <https://doi.org/10.1088/1361-6463/50/5/053002>.
- [17] R. Skini, A. Omri, M. Khelifi, E. Dhahri, E.K. Hlil, Large magnetocaloric effect in lanthanum-deficiency manganites $\text{La}_{0.8-x}\text{Ca}_{0.2}\text{MnO}_3$ ($0.00 \leq x \leq 0.20$) with a first-order magnetic phase transition, *J. Magn. Magn. Mater.* 364 (2014) 5–10. <https://doi.org/10.1016/j.jmmm.2014.04.009>.
- [18] M.S. Anwar, F. Ahmed, G.W. Kim, S.N. Heo, B.H. Koo, The interplay of Ca and Sr in the bulk magnetocaloric $\text{La}_{0.7}\text{Sr}_{(0.3-x)}\text{Ca}_x\text{MnO}_3$ ($x = 0, 0.1$ and 0.3) manganite, *J. Korean Phys. Soc.* 62 (2013) 1974–1978. <https://doi.org/10.3938/jkps.62.1974>.
- [19] M. Fries, T. Gottschall, F. Scheibel, L. Pfeuffer, K.P. Skokov, I. Skourski, M. Acet, M. Farle, J. Wosnitza, O. Gutfleisch, Dynamics of the magnetoelastic phase transition and adiabatic temperature change in $\text{Mn}_{1.3}\text{Fe}_{0.7}\text{P}_{0.5}\text{Si}_{0.55}$, *J. Magn. Magn. Mater.* 477 (2019) 287–291. <https://doi.org/10.1016/j.jmmm.2018.12.086>.
- [20] M. Ghorbani Zavareh, C. Salazar Mejía, A.K. Nayak, Y. Skourski, J. Wosnitza, C. Felser, M. Nicklas, Direct measurements of the magnetocaloric effect in pulsed magnetic fields: The example of the Heusler alloy $\text{Ni}_{50}\text{Mn}_{35}\text{In}_{15}$, *Appl. Phys. Lett.* 106 (2015) 071904. <https://doi.org/10.1063/1.4913446>.
- [21] C. Salazar Mejía, M. Ghorbani Zavareh, A.K. Nayak, Y. Skourski, J. Wosnitza, C. Felser, M.

- Nicklas, Pulsed high-magnetic-field experiments: New insights into the magnetocaloric effect in Ni-Mn-In Heusler alloys, *J. Appl. Phys.* 117 (2015) 17E710.
<https://doi.org/10.1063/1.4916556>.
- [22] T. Kihara, X. Xu, W. Ito, R. Kainuma, M. Tokunaga, Direct measurements of inverse magnetocaloric effects in metamagnetic shape-memory alloy NiCoMnIn, *Phys. Rev. B.* 90 (2014) 214409. <https://doi.org/10.1103/PhysRevB.90.214409>.
- [23] M.G. Zavareh, Y. Skourski, K.P. Skokov, D.Y. Karpenkov, L. Zvyagina, A. Waske, D. Haskel, M. Zhernenkov, J. Wosnitza, O. Gutfleisch, Direct Measurement of the Magnetocaloric Effect in $\text{La}(\text{Fe,Si,Co})_{13}$ Compounds in Pulsed Magnetic Fields, *Phys. Rev. Appl.* 8 (2017) 014037. <https://doi.org/10.1103/PhysRevApplied.8.014037>.
- [24] G.C. Lin, Q. Wei, J.X. Zhang, Direct measurement of the magnetocaloric effect in $\text{La}_{0.67}\text{Ca}_{0.33}\text{MnO}_3$, *J. Magn. Magn. Mater.* 300 (2006) 392–396.
<https://doi.org/10.1016/j.jmmm.2005.05.023>.
- [25] H.J. Whitlow, G. Possnert, C.S. Petersson, Quantitative mass and energy dispersive elastic recoil spectrometry: Resolution and efficiency considerations, *Nucl. Inst. Methods Phys. Res. B.* 27 (1987) 448–457. [https://doi.org/10.1016/0168-583X\(87\)90527-1](https://doi.org/10.1016/0168-583X(87)90527-1).
- [26] J. Liu, T. Gottschall, K.P. Skokov, J.D. Moore, O. Gutfleisch, Giant magnetocaloric effect driven by structural transitions, *Nat. Mater.* 11 (2012) 620–626.
<https://doi.org/10.1038/nmat3334>.
- [27] R. Young, *The Rietveld Method*, IUCr, International Union of Crystallography, 1993.
<https://www.worldcat.org/title/rietveld-method/oclc/26299196> (accessed July 26, 2019).
- [28] Y. Tokura, Y. Tomioka, Colossal magnetoresistive manganites, *J. Magn. Magn. Mater.* 200 (1999) 1–23. [https://doi.org/10.1016/S0304-8853\(99\)00352-2](https://doi.org/10.1016/S0304-8853(99)00352-2).
- [29] L.B. McCusker, R.B. Von Dreele, D.E. Cox, D. Louër, P. Scardi, Rietveld refinement guidelines, *J. Appl. Crystallogr.* 32 (1999) 36–50.
<https://doi.org/10.1107/S0021889898009856>.
- [30] Y. Wang, J. Shao, Y. Yu, Q. Shi, Y. Zhu, T. Miao, H. Lin, L. Xiang, Q. Li, P. Cai, W. Wang, L. Yin, J. Shen, Enhanced magnetocaloric effect in manganite nanodisks, *Phys. Rev. Mater.* 3 (2019) 84411. <https://doi.org/10.1103/PhysRevMaterials.3.084411>.
- [31] M.A. Langell, C.W. Hutchings, G.A. Carson, M.H. Nassir, High resolution electron energy loss spectroscopy of MnO(100) and oxidized MnO(100), *J. Vac. Sci. Technol. A Vacuum, Surfaces, Film.* 14 (1996) 1656–1661. <https://doi.org/10.1116/1.580314>.
- [32] A.T. Kozakov, A.G. Kochur, L.A. Reznichenko, L.A. Shilkina, A.V. Pavlenko, A.V. Nikolskii, K.A. Googlev, V.G. Smotrakov, Single-crystal rare earths manganites $\text{La}_{1-x-y}\text{Bi}_x\text{AyMn}\alpha\text{O}_{3\pm\beta}$ (A=Ba, Pb): Crystal structure, composition, and Mn ions valence state. X-ray diffraction and XPS study, *J. Electron Spectros. Relat. Phenomena.* 186 (2013) 14–24. <https://doi.org/10.1016/j.elspec.2013.01.016>.

- [33] G.D. Dwivedi, A.G. Joshi, S. Kumar, H. Chou, K.S. Yang, D.J. Jhong, W.L. Chan, A.K. Ghosh, S. Chatterjee, Electronic structure study of wide band gap magnetic semiconductor (La_{0.6}Pr_{0.4})_{0.65}Ca_{0.35}MnO₃ nanocrystals in paramagnetic and ferromagnetic phases, *Appl. Phys. Lett.* 108 (2016) 172402. <https://doi.org/10.1063/1.4947466>.
- [34] E. Beyreuther, S. Grafström, L.M. Eng, C. Thiele, K. Dörr, XPS investigation of Mn valence in lanthanum manganite thin films under variation of oxygen content, *Phys. Rev. B.* 73 (2006) 155425. <https://doi.org/10.1103/PhysRevB.73.155425>.
- [35] X. Ning, Z. Wang, Z. Zhang, Fermi Level shifting, Charge Transfer and Induced Magnetic Coupling at La_{0.7}Ca_{0.3}MnO₃/LaNiO₃ Interface, *Sci. Rep.* 5 (2015) 8460. <https://doi.org/10.1038/srep08460>.
- [36] Y.X. Fang, H. Zhang, F. Azad, S.P. Wang, F.C.C. Ling, S.C. Su, Band offset and an ultra-fast response UV-VIS photodetector in γ -In₂Se₃/p-Si heterojunction heterostructures, *RSC Adv.* 8 (2018) 29555–29561. <https://doi.org/10.1039/C8RA05677C>.
- [37] X. Ning, Z. Wang, Z. Zhang, Fermi Level shifting, Charge Transfer and Induced Magnetic Coupling at La_{0.7}Ca_{0.3}MnO₃/LaNiO₃ Interface, *Sci. Rep.* 5 (2015) 8460. <https://doi.org/10.1038/srep08460>.
- [38] C. Schlueter, P. Orgiani, T.-L. Lee, A.Y. Petrov, A. Galdi, B.A. Davidson, J. Zegenhagen, C. Aruta, Evidence of electronic band redistribution in La_{0.65}Sr_{0.35}MnO_{3- δ} by hard x-ray photoelectron spectroscopy, *Phys. Rev. B.* 86 (2012) 155102. <https://doi.org/10.1103/PhysRevB.86.155102>.
- [39] K. Arstila, J. Julin, M.I. Laitinen, J. Aalto, T. Konu, S. Kärkkäinen, S. Rahkonen, M. Raunio, J. Itkonen, J.P. Santanen, T. Tuovinen, T. Sajavaara, Potku - New analysis software for heavy ion elastic recoil detection analysis, *Nucl. Instruments Methods Phys. Res. Sect. B Beam Interact. with Mater. Atoms.* 331 (2014) 34–41. <https://doi.org/10.1016/j.nimb.2014.02.016>.
- [40] M. Mayer, SIMNRA, a simulation program for the analysis of NRA, RBS and ERDA, in: *AIP Conf. Proc.*, AIP, 2008: pp. 541–544. <https://doi.org/10.1063/1.59188>.
- [41] M.S. Anwar, F. Ahmed, G.W. Kim, S.N. Heo, B.H. Koo, The interplay of Ca and Sr in the bulk magnetocaloric La_{0.7}Sr_(0.3-x)Ca_xMnO₃ (x = 0, 0.1 and 0.3) manganite, *J. Korean Phys. Soc.* 62 (2013) 1974–1978. <https://doi.org/10.3938/jkps.62.1974>.
- [42] R. Skini, M. Khelifi, E.K. Hlil, An efficient composite magnetocaloric material with a tunable temperature transition in K-deficient manganites, *RSC Adv.* 6 (2016) 34271–34279. <https://doi.org/10.1039/C5RA27132K>.
- [43] F.-X. Hu, B.-G. Shen, J.-R. Sun, Z.-H. Cheng, G.-H. Rao, X.-X. Zhang, Influence of negative lattice expansion and metamagnetic transition on magnetic entropy change in the compound LaFe_{11.4}Si_{1.6}, *Appl. Phys. Lett.* 78 (2001) 3675–3677. <https://doi.org/10.1063/1.1375836>.
- [44] T. Krenke, E. Duman, M. Acet, E.F. Wassermann, X. Moya, L. Mañosa, A. Planes, Inverse magnetocaloric effect in ferromagnetic Ni–Mn–Sn alloys, *Nat. Mater.* 4 (2005) 450–454.

- <https://doi.org/10.1038/nmat1395>.
- [45] V.K. Pecharsky, K.A. Gschneidner, Jr., Giant Magnetocaloric Effect in $\text{Gd}_5(\text{Si}_2\text{Ge}_2)$, *Phys. Rev. Lett.* 78 (1997) 4494–4497. <https://doi.org/10.1103/PhysRevLett.78.4494>.
- [46] M. Wali, R. Skini, M. Khelifi, E. Dhahri, E.K. Hlil, A giant magnetocaloric effect with a tunable temperature transition close to room temperature in Na-deficient $\text{La}_{0.8}\text{Na}_{0.2-x}\text{MnO}_3$ manganites, *Dalt. Trans.* 44 (2015) 12796. <https://doi.org/10.1039/c5dt01254f>.
- [47] R. Skini, A. Omri, M. Khelifi, E. Dhahri, E.K. Hlil, Large magnetocaloric effect in lanthanum-deficiency manganites $\text{La}_{0.8-x}\text{Ca}_{0.2}\text{MnO}_3$ ($0.00 \leq x \leq 0.20$) with a first-order magnetic phase transition, *J. Magn. Magn. Mater.* 364 (2014) 5–10. <https://doi.org/10.1016/j.jmmm.2014.04.009>.
- [48] V.K. Pecharsky, K.A. Gschneidner, Magnetocaloric effect from indirect measurements: Magnetization and heat capacity ARTICLES YOU MAY BE INTERESTED IN, *J. Appl. Phys.* 86 (1999) 565. <https://doi.org/10.1063/1.370767>.
- [49] P. Nikkola, C. Mahmed, M. Balli, O. Sari, 1D model of an active magnetic regenerator, *Int. J. Refrig.* 37 (2014) 43–50. <https://doi.org/10.1016/j.ijrefrig.2013.09.026>.
- [50] A.G. Gamzatov, A.M. Aliev, P.D.H. Yen, K.X. Hau, K.E. Kamaludinova, T.D. Thanh, N.T. Dung, S.-C. Yu, Magnetocaloric effect in $\text{La}_{0.7-x}\text{Pr}_x\text{Sr}_{0.3}\text{MnO}_3$ manganites: Direct and indirect measurements, *J. Magn. Magn. Mater.* 474 (2019) 477–481. <https://doi.org/10.1016/j.jmmm.2018.11.017>.
- [51] K. Riahi, I. Messaoui, A. Ezaami, F. Cugini, M. Solzi, W. Cheikhrouhou-Koubaa, A. Cheikhrouhou, Adiabatic temperature change, magnetic entropy change and critical behavior near the ferromagnetic–paramagnetic phase transition in $\text{La}_{0.7}(\text{Ca},\text{Sr})_{0.3}\text{MnO}_3$ perovskite, *Phase Transitions.* 91 (2018) 691–702. <https://doi.org/10.1080/01411594.2018.1474356>.
- [52] A. Arrott, J.E. Noakes, Approximate Equation of State For Nickel Near its Critical Temperature, *Phys. Rev. Lett.* 19 (1967) 786–789. <https://doi.org/10.1103/PhysRevLett.19.786>.
- [53] S.S. Samatham, V. Ganesan, Critical behavior, universal magnetocaloric, and magnetoresistance scaling of MnSi , *Phys. Rev. B.* 95 (2017) 115118. <https://doi.org/10.1103/PhysRevB.95.115118>.
- [54] S. Ghorai, S.A. Ivanov, R. Skini, P. Svedlindh, Evolution of Griffiths Phase and Critical Behaviour of $\text{La}_{1-x}\text{Pb}_x\text{MnO}_{3+y}$ Solid Solutions, (2020). <http://arxiv.org/abs/2003.10207> (accessed April 13, 2020).
- [55] A. Smith, K.K. Nielsen, C.R.H. Bahl, Scaling and universality in magnetocaloric materials, *Phys. Rev. B.* 90 (2014) 104422. <https://doi.org/10.1103/PhysRevB.90.104422>.
- [56] V. Franco, A. Conde, Scaling laws for the magnetocaloric effect in second order phase transitions: From physics to applications for the characterization of materials, *Int. J. Refrig.* 33

- (2010) 465–473. <https://doi.org/10.1016/j.ijrefrig.2009.12.019>.
- [57] P.T. Phong, L.T.T. Ngan, L. V. Bau, N.X. Phuc, P.H. Nam, L.T.H. Phong, N. V. Dang, I.J. Lee, Magnetic field dependence of Griffith phase and critical behavior in La_{0.8}Ca_{0.2}MnO₃ nanoparticles, *J. Magn. Magn. Mater.* 475 (2019) 374–381. <https://doi.org/10.1016/j.jmmm.2018.11.122>.
- [58] D. Kim, B.L. Zink, F. Hellman, J.M.D. Coey, Critical behavior of La_{0.75}Sr_{0.25}MnO₃, *Phys. Rev. B.* 65 (2002) 214424. <https://doi.org/10.1103/PhysRevB.65.214424>.
- [59] A. K. Heilman et al., Field-Induced Crossover in La_{0.7}Pb_{0.3}MnO₃, *Phys. C.* 348 (2000) 707–710.
- [60] J.Y. Law, V. Franco, L.M. Moreno-Ramírez, A. Conde, D.Y. Karpenkov, I. Radulov, K.P. Skokov, O. Gutfleisch, A quantitative criterion for determining the order of magnetic phase transitions using the magnetocaloric effect, *Nat. Commun.* 9 (2018) 2680. <https://doi.org/10.1038/s41467-018-05111-w>.
- [61] Y. Xie, J. Fan, L. Xu, X. Zhang, R. Xu, Y. Zhu, R. Tang, C. Wang, C. Ma, L. Pi, Y. Zhang, H. Yang, Unambiguous determining the Curie point in perovskite manganite with second-order phase transition by scaling method, *Phys. Lett. A.* 383 (2019) 125843. <https://doi.org/10.1016/j.physleta.2019.125843>.